

Explaining Excess Dipole in NVSS Data Using Superhorizon Perturbation

Kaustav K. Das,^{a,b} Kishan Sankharva,^a Pankaj Jain^a

^aDepartment of Physics, Indian Institute of Technology Kanpur, Uttar Pradesh - 208016

^bDivision of Physics, Mathematics, and Astronomy, California Institute of Technology, Pasadena, CA 91125, USA

E-mail: kdas@astro.caltech.edu, kishans@iitk.ac.in, pkjain@iitk.ac.in

Abstract. Many observations in recent times have shown evidence against the standard assumption of isotropy in the Big Bang model. Introducing a superhorizon scalar metric perturbation has been able to explain some of these anomalies. In this work, we probe the net velocity arising due to the perturbation, which does not cancel out for large scale structure, unlike in the case of CMB. Thus, within this model's framework, our velocity with respect to the CMB is different from the velocity with respect to the large scale structure. Taking this extra velocity component into account, we study the superhorizon mode's implications for the excess dipole observed in the NRAO VLA Sky Survey (NVSS). We find that the mode can consistently explain both the CMB and NVSS observations. We also find that the model is consistent with the observed Hubble constant dipole and the Hubble bulk flow velocity. The model leads to several predictions which can be tested in future surveys. In particular, it implies that the observed dipole in large scale structure should be redshift dependent and should show an increase in amplitude with redshift. We also find that the Hubble parameter should show a dipole anisotropy whose amplitude must increase with redshift in the CMB frame. Similar anisotropic behaviour is expected for the observed redshift as a function of the luminosity distance.

Keywords: cosmology of theories beyond the SM, CMBR theory, high redshift galaxies, cosmic flows

Contents

1	Introduction	1
2	Our Velocity with respect to the Large Scale Structure	3
3	Gravitational Redshift: SW and ISW Effect due to the Superhorizon Perturbation	6
4	Overdensity of Matter due to the Superhorizon Perturbation	6
5	Modeling Dipole Anisotropy in Large Scale Structure	7
5.1	Kinematic Dipole	9
5.2	Gravitational Dipole	9
5.3	Intrinsic Dipole	9
6	Fitting the Observed NVSS Dipole	10
7	Dipole Anisotropy in Hubble Constant and Bulk Flow Observations	12
7.1	Hubble Constant Dipole in COMPOSITE Sample	14
7.2	Bulk Flow Observations	14
8	Signatures of the Model to be Tested in Future	14
8.1	Dipole Distribution in Galaxy Surveys	15
8.2	Radio Dipole Prediction for Higher Redshifts	16
8.3	Predictions for Anisotropy in the Observed Redshift	17
9	Conclusion	18

1 Introduction

The most widely accepted model of cosmology is the standard Λ CDM cosmology. It explains many cosmological observations, including the cosmic microwave background (CMB) and the primordial ${}^4\text{He}$ abundance. The standard model's core assumption, known as the cosmological principle, is that the universe is homogeneous and isotropic on large distance scales. Within the inflationary big bang model, the universe is expected to become isotropic during the early stages of inflation [1].

Recently, however, there is mounting evidence against the isotropy of the universe. Data from Wilkinson Microwave Anisotropy Probe (WMAP) has shown anomalies such as asymmetry in the CMB power spectrum [2] and alignment of the CMB quadrupole and octupole axes [3]. The Planck data [4] also show similar anomalies. Furthermore, anisotropy has been observed in the propagation of radio polarizations from distant galaxies [5]. Interestingly, the quadrupole-octupole alignment axis, the radio polarization dipole axis, and the CMB dipole axis roughly align along the same direction [6], implying a possible violation of isotropy. The optical polarizations from distant quasars show alignment over large distance scales [7]. This effect also maximizes in the direction of CMB dipole [6].

One way to test the isotropy is to compare our velocity relative to the CMB rest frame with that relative to the large scale structure. If the universe is isotropic, the two velocities should be identical. Our motion relative to the CMB frame gives rise to the CMB dipole signal. This signal has been observed to be of the order of 10^{-3} [8, 9], and predicts our velocity to be around 369 km s^{-1} along the galactic longitude and latitude $(l, b) = (264^\circ, 48^\circ)$ [10, 11]. This local velocity is borne of the gravitational attraction of various massive structure, including the Virgo, the Great Attractor Hydra-Centaurus, Coma, Hercules, and Shapley superclusters, lying along the direction of the CMB dipole.

Our velocity relative to the large scale structure generates a dipole, known as velocity dipole or radio dipole, in the sky brightness and number count of galaxies due to aberration and Doppler effects. Various detailed maps of the local universe, including supernova catalogues, show that the nearby structure cannot account for at least 20% of the CMB dipole value [12–17]. Thus, it is necessary to go beyond our local universe to assert if our velocity with respect to the large scale structure converges to the value predicted by CMB.

Radio astronomy provides an excellent opportunity to probe the universe at large scales. The radio sky surveys, such as the NRAO VLA Sky Survey (NVSS [18]), the Sydney University Molonglo Sky Survey (SUMSS [19]), and the TIFR GMRT Sky Survey (TGSS [20]) have been used to measure our velocity relative to the large scale structure. These radio surveys are relatively wide and deep, peaking at a redshift of $z \approx 1$ [21]. The galaxy clustering at such redshift ranges contributes very little to the dipole if we assume the Λ CDM background power spectrum. However, we expect our local motion to produce Doppler and aberration effects, which leads to a dipole in the radio galaxy distribution [22]. We do observe a dipole in these radio surveys in roughly the same direction as CMB dipole, but surprisingly the magnitude is much higher.

The NVSS is a catalogue of nearly 2 million radio galaxies covering the sky above declination of $\sim -40^\circ$. Various attempts have been made to calculate the radio dipole in the NVSS catalogue and check for convergence to the CMB dipole [23–28]. In almost all the studies, the velocity of our local motion obtained from the NVSS dipole exceeds that obtained from the CMB dipole. In [29], it is shown that the NVSS dipole is at least 2.3σ greater than the CMB predicted velocity dipole. This excess dipole and the mismatch in velocity of our local motion could imply that the standard cosmological principle does not hold and that the radio galaxy distribution is anisotropic at large distance scales.

There have been other explanations for the excess velocity dipole without violating the cosmological principle. These include incomplete sky coverage and various systematic errors. Many methods have been adopted to check for coverage completeness and take into account the errors in source fluxes and flux calibration, but the excess dipole still stays. Colin et al. 2017 [30] combined the NVSS and SUMSS data to achieve a full-sky coverage. They reported a dipole signal that is similar in direction and magnitude to that of the NVSS catalogue.

The TGSS catalogue [20], comprising of 0.62 million sources, also predicts a very high dipole signal [31, 32]. However, the dipole signal from TGSS disagrees not only with the CMB predictions, but also with the dipole signal from NVSS. There might be some unknown systematic error present in the TGSS data [33, 34], and so, in this paper, we focus on the higher-than-expected value of the velocity dipole found in the NVSS data and explain it using a model within the framework of Λ CDM cosmology.

It has been suggested that a superhorizon perturbation may be responsible for the observed violations of statistical isotropy [35–38]. Superhorizon implies that the wavelength of the perturbation is greater than the particle horizon. [39] used the superhorizon perturbation

to explain the anomaly in the NVSS data. Such a perturbation has also been invoked to explain the hemispherical power asymmetry in CMB [35, 36].

Following the earlier work [35–39], we assume a superhorizon perturbation to explain the anomalous dipole value in the NVSS data. Unlike previous work in this area [39], we include the following new elements: i) an extra velocity component which arises due to the superhorizon perturbation, ii) contribution to the dipole from gravitational redshift, iii) an evolving, rather than a constant, relationship between the potential and the density perturbation, and iv) the evolution of the amplitude of the perturbation in the epoch of interest which coincides with a transition from a matter-dominated universe to a dark energy-dominated universe. We investigate how well our model explains the observation data. We also make predictions on radio dipole that could be used to test the validity of the model with future surveys. Further, we check if our model is consistent with observed anisotropy in the Hubble constant and the observed bulk flow velocity.

2 Our Velocity with respect to the Large Scale Structure

The presence of a superhorizon scalar perturbation generates a cosmic velocity field, which leads to an additional component in our velocity with respect to the cosmic frame of rest, over and above peculiar (local) velocity. Our local velocity, which arises due to local inhomogeneities in the matter distribution, manifests itself in the CMB dipole. We denote this local velocity by $v_{\text{local}}\hat{z}$, where we have chosen z -axis as the direction of the CMB dipole. The superhorizon mode does not affect this velocity relative to the CMB because the CMB photons get redshifted (blueshifted) as they emerge from the potential well (peak) created by the superhorizon mode, cancelling the blueshift (redshift) due to our motion induced by the mode [40–42]. Thus, \vec{v}_{local} remains unaffected by the existence of this mode. In contrast, as we shall show in this paper, the superhorizon mode does affect our velocity relative to the large scale structure. In order to obtain our total velocity with respect to the large scale structure, we compute the velocity arising from the superhorizon mode and add \vec{v}_{local} to it. We calculate this total velocity in this section.

We consider a scalar perturbation to the flat FLRW metric, which in the Newtonian gauge is given by $ds^2 = -(1 + 2\Psi)dt^2 + a^2(t)(1 - 2\Phi)\delta_{ij}dx^i dx^j$. As the initial condition for Ψ , we choose a single superhorizon mode with amplitude α and wavevector $\vec{k} = \kappa\hat{z}$.

$$\Psi_{\text{p}} = \alpha \sin(\kappa z + \omega). \quad (2.1)$$

Here, ω is a constant phase factor, and ‘p’ in the subscript stands for primordial. This form of perturbation has been motivated by a general expression used in Erickcek et al. 2008 [38]. It was also used in Ghosh 2014 [39] with $\omega = 0$. We have taken the perturbation to lie along the z -axis because the dipole in the NVSS data is found to lie in the direction of our velocity with respect to the CMB [24]. Note that in Eq. 2.1, z is the comoving Cartesian coordinate, and not redshift. Beyond this point, we use z to denote redshift, and $r \cos \theta$ to represent the Cartesian coordinate z . r is the comoving distance from the origin and θ is the polar angle measured with respect to the z -axis.

We use the following simplifications throughout the paper. We assume a universe without anisotropic stress. Hence, the potential Φ in the Newtonian gauge is identical to Ψ . Further, since the perturbation is superhorizon, we assume $\kappa/H_0 \ll 1$, where H_0 is the Hubble constant. For calculations, we assume a Λ CDM model with parameter values: $\Omega_M = 0.3111$, $\Omega_\Lambda = 0.6889$, $z_{\text{eq}} = 3387$ and $H_0 = 67.66 \text{ km s}^{-1} \text{ Mpc}^{-1}$ (from Planck Collaboration 2018

[43]). Here, Ω_M is the matter density parameter, Ω_Λ is the dark energy density parameter, and z_{eq} is the redshift of matter-radiation equality.

It can be shown that during the current epoch, the perturbation as a function of time is given by [38]

$$\Psi(a) = \frac{9}{4} \Psi_p \Omega_M H_0^2 \frac{\tilde{H}(a)}{a} \int_0^a \frac{da'}{[a' \tilde{H}(a')]^3} \quad (2.2)$$

where

$$\tilde{H}^2(a) = H_0^2 \left(\frac{\Omega_M}{a^3} + \Omega_\Lambda \right), \quad (2.3)$$

and $a = 1/(1+z)$ is the scale factor normalised to unity at the current epoch. Eq. 2.2 is valid long after matter-radiation equality ($a(1+z_{\text{eq}}) \gg 1$). Since the NVSS data extends only up to $z = 2$, we use Eq. 2.2 for this work.

The cosmic velocity field generated by the perturbation can be computed via [38]

$$\vec{v}(a, \vec{r}) = -\frac{2a^2}{H_0 \Omega_M} \frac{H(a)}{H_0} \left(\frac{y}{4+3y} \right) \left[\vec{\nabla} \Psi + \frac{d}{d \ln a} \vec{\nabla} \Psi \right] \quad (2.4)$$

where $y = a(1+z_{\text{eq}})$, and

$$H^2(a) = H_0^2 \left[\frac{\Omega_M}{a^4} \left(\frac{1}{1+z_{\text{eq}}} \right) + \frac{\Omega_M}{a^3} + \Omega_\Lambda \right]. \quad (2.5)$$

Using Eq. 2.2 and Eq. 2.4, it is straightforward to show that

$$\vec{v}(z, \vec{r}) \equiv \vec{v}(z, \theta) = -\frac{9}{2} \alpha \frac{\kappa}{H_0} f(z) \cos(\kappa r(z) \cos \theta + \omega) \hat{z} \quad (2.6)$$

where

$$f(z) = (1+z) \frac{y}{4+3y} \frac{H(z)}{\tilde{H}(z)} \left[\frac{H_0}{\tilde{H}(z)} - \frac{3}{2} \Omega_M H_0^3 (1+z) \int_z^\infty \frac{1+z'}{\tilde{H}^3(z')} dz' \right], \quad (2.7)$$

and

$$r(z) = \int_0^z \frac{dz'}{H(z')}. \quad (2.8)$$

Here, we have replaced scale factor a in favour of redshift z .

Our velocity relative to an object at redshift z and polar angle θ can be computed by

$$\vec{v}_{\text{rel}}(z, \theta) = \vec{v}(z=0) - \vec{v}(z, \theta). \quad (2.9)$$

Keeping terms only up to first order in κ/H_0 , we obtain

$$\vec{v}_{\text{rel}}(z) = \frac{9}{2} \alpha \frac{\kappa}{H_0} \cos \omega [f(z) - f(0)] \hat{z}. \quad (2.10)$$

Note that v_{rel} does not depend on θ at the lowest order. This is our velocity relative to an object at redshift z due to the superhorizon mode. In order to obtain our net velocity with

respect to the large scale structure, we add the velocity of the Sun relative to the CMB, which is given by $v_{\text{local}} = (369.0 \pm 0.9) \text{ km s}^{-1}$ along $(l, b) = (263.99^\circ, 48.26^\circ) \pm (0.14^\circ, 0.03^\circ)$ in the galactic coordinates [9]. Then,

$$\vec{v}_{\text{net}}(z) = [v_{\text{rel}}(z) + v_{\text{local}}]\hat{z}. \quad (2.11)$$

$$v_{\text{net}} = \frac{9}{2}[f(z) - f(0)]\alpha \frac{\kappa}{H_0} \cos \omega + v_{\text{local}} \quad (2.12)$$

The velocity distributions given by Eq. 2.10 and Eq. 2.12 are plotted in Figure 1 using $\alpha = 0.381$, $\kappa = 0.043H_0$ and $\omega = \pi$. As we shall see later in § 6, these parameter values correspond to the smallest positive value of α that can explain the NVSS and the CMB data simultaneously. For comparison, we have also plotted the local peculiar velocity of 369 km s^{-1} . Since the smallest plausible value of α is used, Figure 1 shows the minimum theoretical prediction for the bulk flow velocity as a function of redshift.

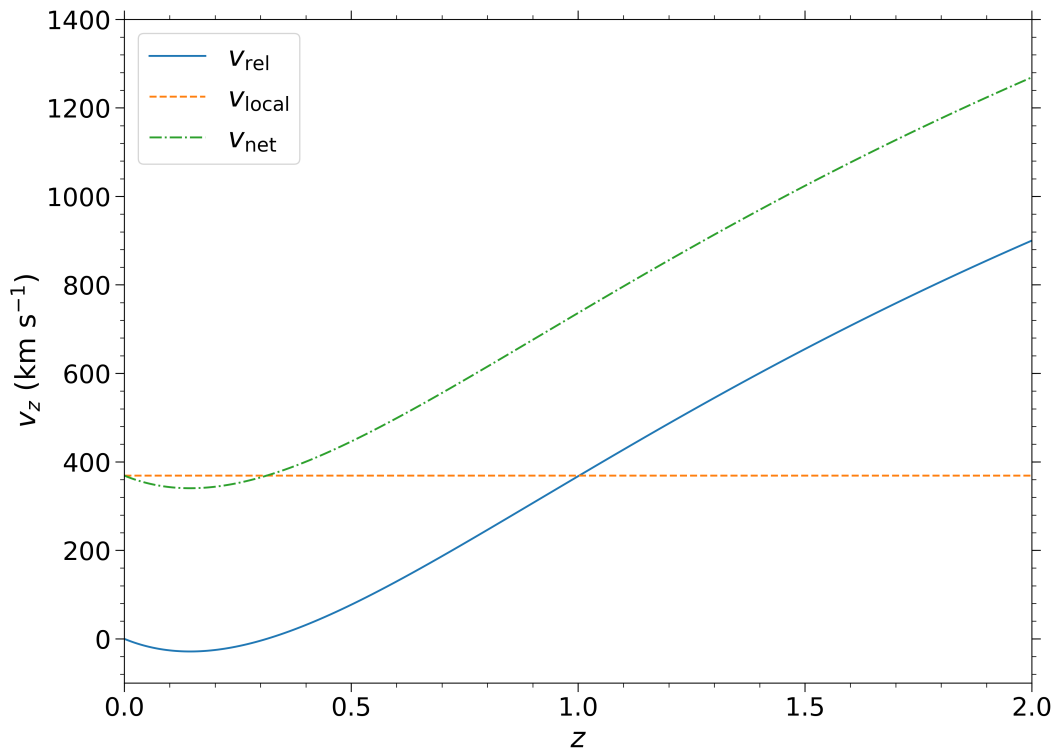


Figure 1. Lower bound on predicted velocity distribution. The orange dotted line represents our velocity relative to the CMB, while the blue solid line represents the velocity obtained via Eq. 2.10 using $\alpha = 0.381$, $\kappa = 0.043H_0$ and $\omega = \pi$. The net velocity (Eq. 2.12) obtained by adding the two components is shown by the dot-dash green line. The velocities are along the z -direction.

3 Gravitational Redshift: SW and ISW Effect due to the Superhorizon Perturbation

The perturbation also leads to a gravitational redshift. We calculate the redshift due to the Sachs-Wolfe (SW) and the integrated Sachs-Wolfe (ISW) effect in this section. The temperature fluctuations of photons due to the SW and the ISW effects, upto first order in κ , are given by

$$\left(\frac{\Delta T}{T}\right)_{\text{SW}} = \Psi(z, \vec{r}) - \Psi(z=0, \vec{r}=\vec{0}) \quad (3.1)$$

and

$$\left(\frac{\Delta T}{T}\right)_{\text{ISW}} = \mathcal{I}_0 \sin \omega + (\mathcal{I}_0 - \mathcal{I}_1) \vec{\kappa} \cdot \vec{r} \cos \omega, \quad (3.2)$$

respectively [38]. \mathcal{I}_n is defined as

$$\mathcal{I}_n = \frac{2\alpha}{r^n} \int_z^0 [r(z) - r(z')]^n \frac{dg}{dz'} dz'. \quad (3.3)$$

Here, we have defined $g(z)$ using $\Psi(z, \vec{r}) = g(z)\Psi_p$, where $\Psi(z, \vec{r})$ is given by Eq. 2.2. The gravitational redshift computed from Eq. 3.1 and Eq. 3.2, upto first order in κ , is given by

$$z_{\text{grav}} = -\left(\frac{\Delta T}{T}\right)_{\text{SW+ISW}} = -\alpha \sin \omega [g(0) - g(z)] + \alpha \kappa \cos \omega \cos \theta r(z) g(z) - 2\alpha \kappa \cos \omega \cos \theta \int_0^z \frac{g(z')}{H(z')} dz'. \quad (3.4)$$

4 Overdensity of Matter due to the Superhorizon Perturbation

In this section, we compute the matter overdensity. In the first order perturbation theory in a flat universe with no entropy perturbations, the potential Ψ and the matter overdensity Δ_M are related during late time via (see Equation 5.27 of Dodelson [44])

$$\Delta_M = -\frac{2a^3}{\Omega_M} \frac{H^2(a)}{H_0^2} \left[\Psi + \frac{d}{d \ln a} \Psi \right] \quad (4.1)$$

where we have neglected radiation and the terms of order κ^2 . Using Eq. 2.2, we can easily show that

$$\Delta_M = -\frac{9}{2} \alpha F(z) \sin(\kappa r \cos \theta + \omega) \quad (4.2)$$

where

$$F(z) = \frac{H^2(z)}{H_0 \tilde{H}(z)} \left[\frac{H_0}{\tilde{H}(z)} - \frac{3}{2} \Omega_M H_0^3 (1+z) \int_z^\infty \frac{1+z'}{\tilde{H}^3(z')} dz' \right]. \quad (4.3)$$

The density perturbations arising from all the other modes in a homogeneous and isotropic universe can simply be added to the above result because we are working in the linear regime [45]. However, in the present study, we work with only the inhomogeneous term, given by Eq. 4.2, because the contribution of the remaining modes to the dipole is expected to be negligible on the distance scale of interest.

5 Modeling Dipole Anisotropy in Large Scale Structure

The radio dipole observed in the large scale structure has three contributions: the kinematic dipole D_{kin} , the gravitational dipole D_{grav} and the intrinsic dipole D_{int} . The kinematic dipole arises as a result of the Doppler and aberration effects due to \vec{v}_{net} – our velocity relative to the large scale structure, while the gravitational dipole results from the Doppler effect due to the gravitational redshift z_{grav} . On the other hand, the intrinsic dipole appears because of the inhomogeneous distribution of matter which is encoded in the overdensity Δ_M . As described earlier, the superhorizon mode contributes to all – D_{kin} , D_{grav} and D_{int} . Here, we determine this additional contribution besides the dipole arising due to our velocity, v_{local} , with respect to the CMB. Since the perturbation is assumed to be a single-mode aligned along the z -axis, all three contributions lie along \hat{z} . Hence, the observed dipole is given by

$$\vec{D}_{\text{obs}} = (D_{\text{kin}} + D_{\text{grav}} + D_{\text{int}})\hat{z}. \quad (5.1)$$

To compute the dipole, consider the flux density of the radio sources assumed to be described by a power law $S(\nu)$ (units: $\text{W m}^{-2} \text{Hz}^{-1}$) depending on frequency ν as

$$S(\nu) \propto \nu^{-\alpha'}. \quad (5.2)$$

Note that there is no relation between α of Eq. 2.1 and α' of Eq. 5.2. The integral source count per unit solid angle above a lower flux limit can also be approximated by a power law (see [27])

$$\frac{dN}{d\Omega}(> S) \propto S^{-x}. \quad (5.3)$$

Here, we take the spectral indices as $x \approx 1$ and $\alpha' \approx 0.75$ [25]. For an observer moving with a velocity $v = v_{\text{net}}$, the Doppler shift in the frequency is $\nu_{\text{obs}} = \nu_{\text{rest}}\delta$, where

$$\delta \approx 1 + v_{\text{net}} \cos \theta \quad (5.4)$$

at leading order. We also need to add the contribution from the gravitational redshift. So, we have $\nu_{\text{obs}} = \nu_{\text{rest}}\delta_1$, where

$$\delta_1 \approx 1 + v_{\text{net}} \cos \theta - z_{\text{grav}}. \quad (5.5)$$

The relation between the observed and the actual flux at a fixed frequency due to the Doppler effect is then given by [22]

$$S_{\text{obs}} = S_{\text{rest}}\delta_1^{1+\alpha'}. \quad (5.6)$$

Furthermore, the aberration effect changes the solid angle in the direction of motion according to $d\Omega_{\text{obs}} = d\Omega_{\text{rest}}\delta^{-2}$.

Let d^2N_{rest} and d^2N_{obs} represent the number of sources in the bin $d\Omega_{\text{rest}}dS_{\text{rest}}$ and $d\Omega_{\text{obs}}dS_{\text{obs}}$, respectively. From Eq. 5.3, we find

$$\frac{d^2N_{\text{rest}}}{d\Omega_{\text{rest}}dS_{\text{rest}}} = kx(S_{\text{rest}})^{-1-x} \quad (5.7)$$

where k is a proportionality constant. We have $d^2N_{\text{rest}} = d^2N_{\text{obs}}$, and therefore, we obtain

$$d^2N_{\text{obs}} = d^2N_{\text{rest}} = kx(S_{\text{rest}})^{-1-x}\delta^2d\Omega_{\text{obs}}dS_{\text{rest}}. \quad (5.8)$$

Substituting S_{rest} from Eq. 5.6, we obtain

$$d^2 N_{\text{obs}} = kx(S_{\text{obs}})^{-1-x} \delta_1^{x(1+\alpha')} \delta^2 d\Omega_{\text{obs}} dS_{\text{obs}}. \quad (5.9)$$

Integrating over S_{obs} from S_{low} to ∞ , we get

$$\left(\frac{dN}{d\Omega}\right)_{\text{obs}} = k(S_{\text{low}})^{-x} \delta^2 \delta_1^{x(1+\alpha')} = \left(\frac{dN}{d\Omega}\right)_{\text{rest}} \delta^2 \delta_1^{x(1+\alpha')}. \quad (5.10)$$

We point out that each of the terms $(dN/d\Omega)_{\text{obs}}$, $(dN/d\Omega)_{\text{rest}}$ and $\delta^2 \delta_1^{x(1+\alpha')}$ can be a function of redshift z in addition to θ and ϕ (the polar angles). We can express $(dN/d\Omega)_{\text{rest}}$ as

$$\left(\frac{dN}{d\Omega}\right)_{\text{rest}} = \left(\frac{dN}{d\Omega}\right)_{\text{rest}}^{(0)} + \Delta \left(\frac{dN}{d\Omega}\right)_{\text{rest}} \quad (5.11)$$

where $(dN/d\Omega)_{\text{rest}}^{(0)}$ is the isotropic zeroth order term and $\Delta(dN/d\Omega)_{\text{rest}}$ is a perturbation to the zeroth order term. Note that $(dN/d\Omega)_{\text{rest}}^{(0)} \propto \rho_M$ and $\Delta(dN/d\Omega)_{\text{rest}} \propto \delta\rho_M(\theta, \phi)$. Hence, we can write

$$\frac{(dN/d\Omega)_{\text{rest}}}{(dN/d\Omega)_{\text{rest}}^{(0)}} = 1 + \Delta_M. \quad (5.12)$$

$\Delta_M = \delta\rho_M/\rho_M$ is the matter overdensity. Dividing Eq. 5.10 by $(dN/d\Omega)_{\text{rest}}^{(0)}$, we get

$$\frac{(dN/d\Omega)_{\text{obs}}}{(dN/d\Omega)_{\text{rest}}^{(0)}} = (1 + \Delta_M) \delta^2 \delta_1^{x(1+\alpha')}. \quad (5.13)$$

We expand $\delta^2 \delta_1^{x(1+\alpha')}$ up to first order in $\cos\theta$

$$\delta^2 \delta_1^{x(1+\alpha')} = 1 + v_{\text{net}}[2 + x(1 + \alpha')] \cos\theta - z_{\text{grav}}x(1 + \alpha') \quad (5.14)$$

Therefore,

$$\frac{(dN/d\Omega)_{\text{obs}}}{(dN/d\Omega)_{\text{int}}^{(0)}} = 1 + v_{\text{net}}[2 + x(1 + \alpha')] \cos\theta - z_{\text{grav}}x(1 + \alpha') + \Delta_M \quad (5.15)$$

where we have retained terms up to first order in κ/H_0 only. The coefficient of $\cos\theta$ in the second, third and fourth terms on the right hand side of the above equation leads to D_{kin} , D_{grav} and D_{int} , respectively.

To compute the dipole amplitude, we calculate the spherical harmonic coefficients a_{lm} which, for a general function $f(\theta, \phi)$, are given by

$$a_{lm} = \int f(\theta, \phi) Y_{lm}^*(\theta, \phi) d\Omega. \quad (5.16)$$

The $l = 1$ components represent the dipole. Due to our choice of coordinate system, $a_{11} = 0 = a_{1,-1}$. Thus, we only need to evaluate a_{10} . The dipole amplitude D is computed using [25, 39]

$$D = a_{10} \sqrt{\frac{3}{4\pi}}. \quad (5.17)$$

The dipole, thus obtained, has a dependence on redshift. In order to get the projected dipole value \bar{D} , we multiply D with the normalised galaxy distribution function $w(z)$ of the survey under study and integrate over the redshift range (z_1 to z_2) over which the survey data extends.

$$\bar{D} = \int_{z_1}^{z_2} D(z)w(z)dz. \quad (5.18)$$

5.1 Kinematic Dipole

The kinematic dipole results from the second term in Eq. 5.15. Using Eq. 2.12 and Eq. 5.17, we obtain

$$D_{\text{kin}}(z) = \frac{9}{2}[2 + x(1 + \alpha')][f(z) - f(0)]\alpha \frac{\kappa}{H_0} \cos \omega + v_{\text{local}}[2 + x(1 + \alpha')]. \quad (5.19)$$

This leads to the following value of projected dipole

$$\bar{D}_{\text{kin}} = \mathcal{A}_1(z_1, z_2)\alpha \frac{\kappa}{H_0} \cos \omega + \mathcal{B} \quad (5.20)$$

where

$$\mathcal{A}_1(z_1, z_2) = \frac{9}{2}[2 + x(1 + \alpha')] \left[\int_{z_1}^{z_2} f(z)w(z)dz - f(0) \right] \quad (5.21)$$

and

$$\mathcal{B} = v_{\text{local}}[2 + x(1 + \alpha')]. \quad (5.22)$$

5.2 Gravitational Dipole

The third term on RHS of Eq. 5.15 gives rise to the gravitational dipole. Using Eq. 3.4 and Eq. 5.17, we find

$$D_{\text{grav}}(z) = -x(1 + \alpha') \left[\alpha \kappa \cos \omega r(z)g(z) - 2\alpha \kappa \cos \omega \int_0^z \frac{g(z')}{H(z')} dz' \right]. \quad (5.23)$$

Thus, the projected dipole is given by

$$\bar{D}_{\text{grav}} = \mathcal{A}_2(z_1, z_2)\alpha \frac{\kappa}{H_0} \cos \omega \quad (5.24)$$

where

$$\mathcal{A}_2(z_1, z_2) = -x(1 + \alpha')H_0 \int_{z_1}^{z_2} \left[r(z)g(z) - 2 \int_0^z \frac{g(z')}{H(z')} dz' \right] w(z)dz. \quad (5.25)$$

5.3 Intrinsic Dipole

The intrinsic dipole arises due to the matter overdensity Δ_M . Expanding Eq. 4.2 up to first order in κ , and using Eq. 5.17, we obtain

$$D_{\text{int}}(z) = -\frac{9}{2}r(z)F(z)\alpha \kappa \cos \omega. \quad (5.26)$$

Author	Dipole Amplitude D_{obs}
Tiwari et al. (Number count)[27]	0.0151 ± 0.0030
Tiwari et al. (Sky Brightness) [27]	0.0166 ± 0.0031
Singal [24]	0.019 ± 0.004
Gibelyou and Heutrer [25]	0.027 ± 0.005
Rubart and Schwarz [26]	0.018 ± 0.006
Bengaly et al. [31]	0.0234 ± 0.0039

Table 1. Net observed dipole amplitudes.

The corresponding projected dipole is

$$\bar{D}_{\text{int}} = \mathcal{C}(z_1, z_2) \alpha \frac{\kappa}{H_0} \cos \omega, \quad (5.27)$$

where

$$\mathcal{C}(z_1, z_2) = -\frac{9}{2} H_0 \int_{z_1}^{z_2} r(z) F(z) w(z) dz. \quad (5.28)$$

Adding the three contributions, the net projected dipole is given by

$$\vec{D}_{\text{obs}} = \left[\{ \mathcal{A}_1(z_1, z_2) + \mathcal{A}_2(z_1, z_2) + \mathcal{C}(z_1, z_2) \} \alpha \frac{\kappa}{H_0} \cos \omega + \mathcal{B} \right] \hat{z}. \quad (5.29)$$

This is the predicted value of dipole in the presence of the superhorizon mode.

6 Fitting the Observed NVSS Dipole

The observed NVSS dipole amplitudes are given in Table 1. The spread in values arise due to different methodology employed for extracting the dipole. In particular, Tiwari et al. [27] obtain lower value since they eliminate nearby sources which may bias the cosmological signal. We fit our model to the observed NVSS dipole values while simultaneously satisfying the constraints imposed by CMB on the model parameters. We use the following normalized galaxy distribution function of the NVSS catalogue [29] to compute the projected dipole values

$$w(z) = \mathcal{N} z^{0.74} \exp \left[- \left(\frac{z}{0.71} \right)^{1.06} \right]. \quad (6.1)$$

Here, \mathcal{N} is a normalization constant.

The NVSS data extends over the redshift range $z_1 = 0$ to $z_2 = 2$. Hence, we obtain

$$\alpha \cos \omega = \frac{H_0}{\kappa} \frac{D_{\text{obs}} - \mathcal{B}}{\mathcal{A}_1(0, 2) + \mathcal{A}_2(0, 2) + \mathcal{C}(0, 2)} \quad (6.2)$$

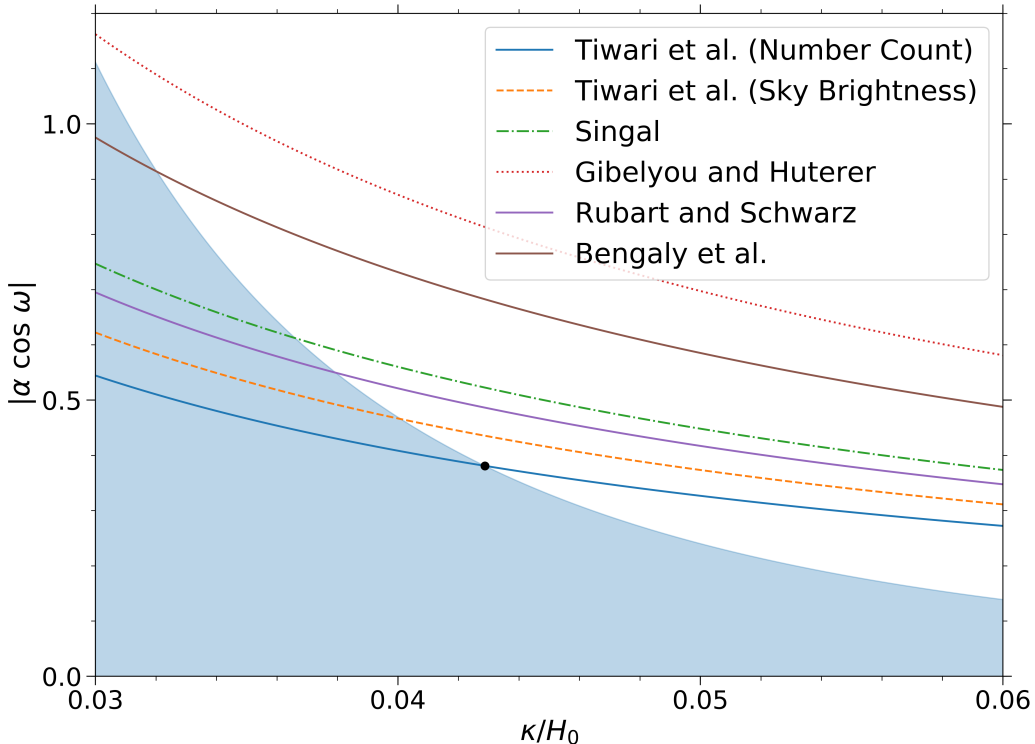


Figure 2. Plot of $|\alpha \cos \omega|$ versus κ/H_0 for the observed NVSS dipole amplitudes. The blue-shaded part denotes the region of parameter space that satisfies the CMB constraint (Eq. 6.3). The black dot at the point $(\alpha, \kappa/H_0, \omega) = (0.381, 0.043, \pi)$ represents the minimum fit value of α .

from Eq. 5.29. In Figure 2, we plot $|\alpha \cos \omega|$ as a function of κ/H_0 for the six values of D_{obs} given in Table 1. The blue-shaded part denotes the region of parameter space that satisfies the CMB constraint [38]

$$|\kappa^3 \alpha \cos \omega| \leq 2.99 \times 10^{-5} H_0^3. \quad (6.3)$$

The errors for the predicted values of α are shown in Figure 3.

We find that there exist model parameter values that fall within the region allowed by the CMB constraint while also explaining the NVSS dipole. Thus, we find that the model provides an explanation for both the NVSS and the CMB data. We note that the model is unable to fit the NVSS dipole value obtained in Gibelyou and Huterer 2012 [25] for α less than 1. The black dot in Figure 2 at the point $(\alpha, \kappa/H_0, \omega) = (0.381, 0.043, \pi)$ represents the minimum fit value of α , that is, the point in the parameter space with the least value of α such that it satisfies both the CMB and the NVSS constraints. Henceforth, we shall use the parameter values corresponding to this minimum fit value to make predictions.

The value of α required is larger in comparison to what was obtained in Ghosh 2014 [39]. This is primarily due to our inclusion of the contribution due to gravitational redshift z_{grav} to the dipole. As expected, this contribution is opposite in sign compared to the kinematic and intrinsic dipoles. The value of α is somewhat large but still small enough so that the mode

may be treated perturbatively. In any case, since the precise value of the dipole is likely to be revised in future observations, we postpone a more ambitious study of including non-linear effects in the predicted dipole to future research.

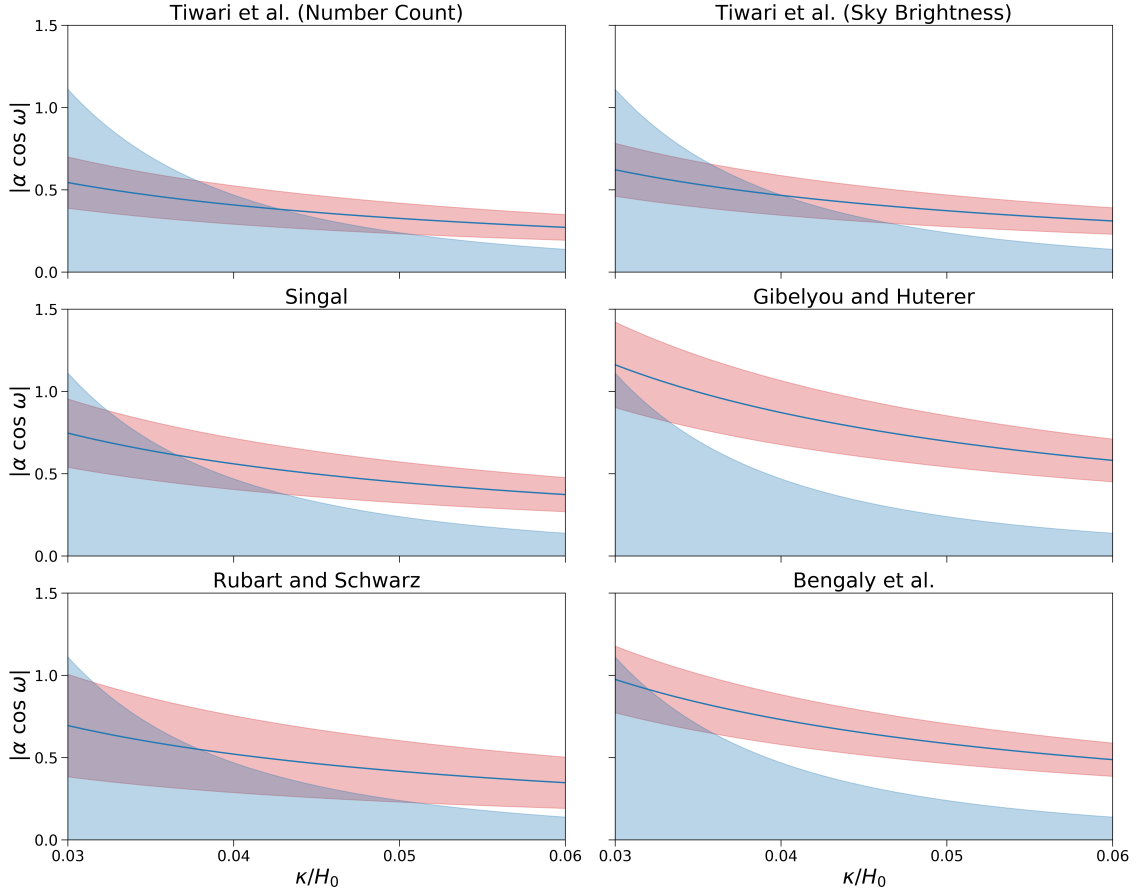


Figure 3. The 1σ confidence contours in $|\alpha \cos \omega|$ versus κ/H_0 space plotted using the dipole amplitudes and errors given in Table 1. The blue-shaded region denotes the region of parameter space that satisfies the CMB constraint (Eq. 6.3).

7 Dipole Anisotropy in Hubble Constant and Bulk Flow Observations

The superhorizon perturbation also affects the redshift of distant sources due to the Doppler and gravitational effects. This will lead to a dipole anisotropy in the Hubble flow. We predict the magnitude of Hubble dipole using our model. Let z be the cosmological redshift in the absence of the superhorizon perturbation. The perturbation gives rise to z_{Doppler} , the Doppler redshift due to our velocity relative to the large scale structure, and z_{grav} , the gravitational redshift due to potential wells and peaks. The observed redshift z_{obs} can then be written as

$$1 + z_{\text{obs}} = (1 + z)(1 + z_{\text{Doppler}})(1 + z_{\text{grav}}). \quad (7.1)$$

The additional contributions, z_{Doppler} and z_{grav} , introduce an anisotropy in the observed redshift. We model this as $z_{\text{obs}} = \bar{z} + \gamma \cos \theta$. Using $z_{\text{Doppler}} = -v_{\text{net}} \cos \theta$, and z_{grav} from Eq.

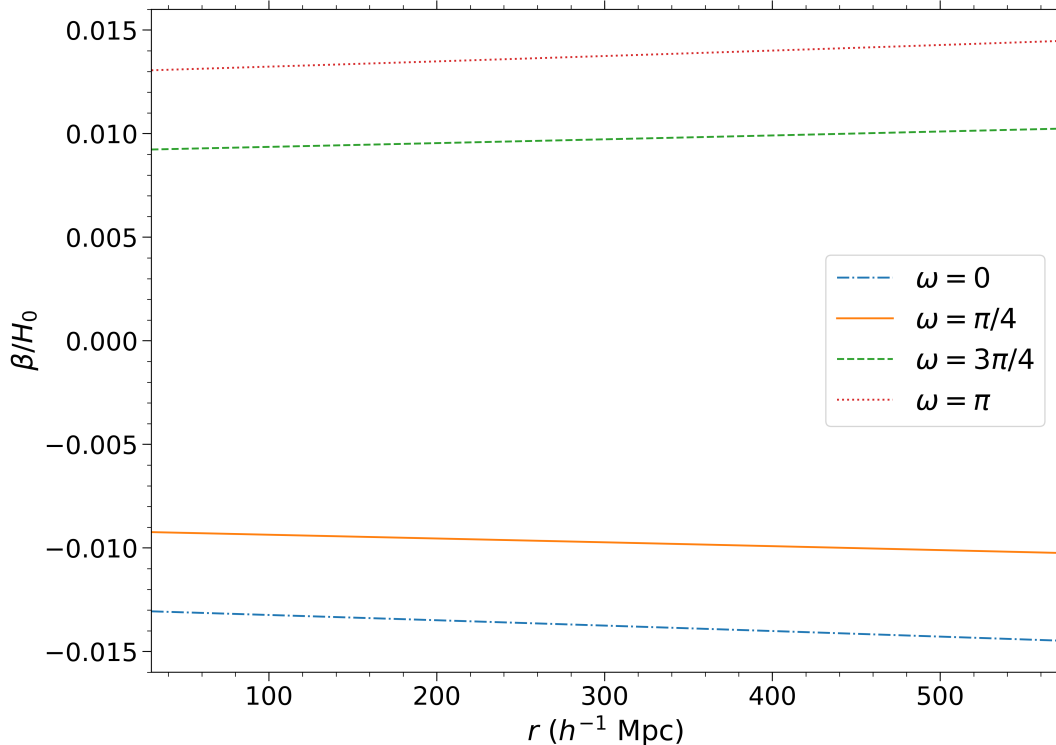


Figure 4. The predicted lower bound on the distribution of Hubble constant dipole $\beta(z)/H_0$ in the CMB rest frame. r is the comoving distance and H_0 is the direction-averaged Hubble constant during the current epoch. The parameter values used are: $(\alpha, \kappa/H_0) = (0.381, 0.043)$ for $\omega = 0, \pi/4, 3\pi/4, \pi$.

3.4, we obtain

$$\bar{z} = z + \alpha \sin \omega (1+z)[g(z) - g(0)] \quad (7.2)$$

and

$$\gamma = \alpha \kappa \cos \omega (1+z) \left[r(z)g(z) - 2 \int_0^z \frac{g(z')}{H(z')} dz' \right] - v_{\text{net}}(1+z)[1 + \alpha \sin \omega \{g(z) - g(0)\}] \quad (7.3)$$

up to first order in κ .

Anisotropy in the observed redshift translates to an anisotropy in the Hubble constant inferred from the observed redshift. We model the observed Hubble constant as $H_0^{\text{obs}} = \bar{H}_0^{\text{obs}} + \beta \cos \theta$. In the local universe, we have $z_{\text{obs}} = H_0^{\text{obs}} r$. Comparing the coefficients of $\cos \theta$, we get

$$\beta(z) = \frac{\gamma}{r(z)}. \quad (7.4)$$

$\beta(z)$ is the dipole component of the observed Hubble constant. It lies along the z -direction. We plot the predicted $\beta(z)/H_0$ in the CMB frame as a function of the comoving distance in Figure 4. For the CMB frame, we use $v_{\text{local}} = 0$ in Eq. 2.12. The parameter values used are: $(\alpha, \kappa/H_0) = (0.381, 0.043)$ for $\omega = 0, \pi/4, 3\pi/4, \pi$. We note that to explain the excess

NVSS dipole, we need negative value for $\cos\omega$, so that v_{rel} is in the direction $(+\hat{z})$ of the local motion (see Eq 2.10). This gives us a positive kinematic dipole which generates a blueshift. However, for this to happen, we must have an over-density in that direction which creates a potential well, redshifting the photons from $+\hat{z}$. In the case of LSS, the redshift due to potential well dominates and this leads to a positive Hubble anisotropy for us. This explains why we have positive values of β for $\omega = 3\pi/4, \pi$ in Figure 4. One can similarly explain the trends for other values of $\cos\omega$.

7.1 Hubble Constant Dipole in COMPOSITE Sample

The COMPOSITE sample of Watkins, Feldman and Hudson [13, 16] is one of the largest available data set of peculiar velocities of galaxies that extend upto $\sim 100h^{-1}$ Mpc. Wiltshire et al. 2013 [46] use this sample to characterize the anisotropy in the Hubble flow, adopting an analysis methodology independent of any cosmological model assumptions except that a suitably defined average linear Hubble law exists.

They fit a dipole Hubble law in independent radial shells. In Figure 5, we show the lower bound on the predicted Hubble constant dipole, along with the observed value obtained by Wiltshire et al. 2013 [46], in the CMB rest frame. We have used $\alpha = 0.381$ and $\kappa = 0.043H_0$ (the smallest fit value of the amplitude of the perturbation obtain in § 6). We note that the direction of the dipole obtained in Wiltshire et al. 2013 [46] has a high variance.

We find that our lower bound prediction is consistent with the observation since the observed dipole in all the radial shells is greater than the minimum value predicted by the model. The excess observed dipole can be attributed to local effects. We postpone a more detailed analysis of the Hubble constant anisotropy using different data sets, rest frames, and analysis methods, including samples at higher redshifts, to future research.

7.2 Bulk Flow Observations

The gravitational pull of large scale structure gives rise to peculiar velocities of galaxies. It is preferable to study the bulk velocity, that is, the mean peculiar velocity of a large volume of space, to understand the distribution of matter. Averaging peculiar velocity over a large volume removes various non-linear effects affecting the small scales. There have been many attempts to deduce the bulk velocity in the local universe using different samples with redshift ranges varying from $z < 0.05$ to $z < 0.2$. The obtained bulk flow velocities vary from 292 ± 96 km s $^{-1}$ to 188 ± 120 km s $^{-1}$. We refer to [17, 47–52] for more details on the samples and methodology used to obtain these values.

In our model, the bulk flow velocity is given by v_{net} , defined in Eq. 2.11. We obtain a v_{net} of about 341 km s $^{-1}$ using $\alpha = 0.381$, $\kappa = 0.043H_0$ and $\omega = \pi$. This value is roughly in agreement with the observed values of bulk flow velocity reported in the literature; however, it falls a little outside the 1σ limit of the observed velocity 188 ± 120 km s $^{-1}$. An important point to note is that the observed bulk flow velocity is lower than the local velocity of 369 km s $^{-1}$. This can be explained partially by the negative value of v_{rel} for low redshifts, as is evident from Figure 1.

8 Signatures of the Model to be Tested in Future

Our model makes several predictions which can be tested in future. Here, we list some predictions for radio and optical surveys. These primarily use the fact that the predicted dipole anisotropy is redshift dependent.

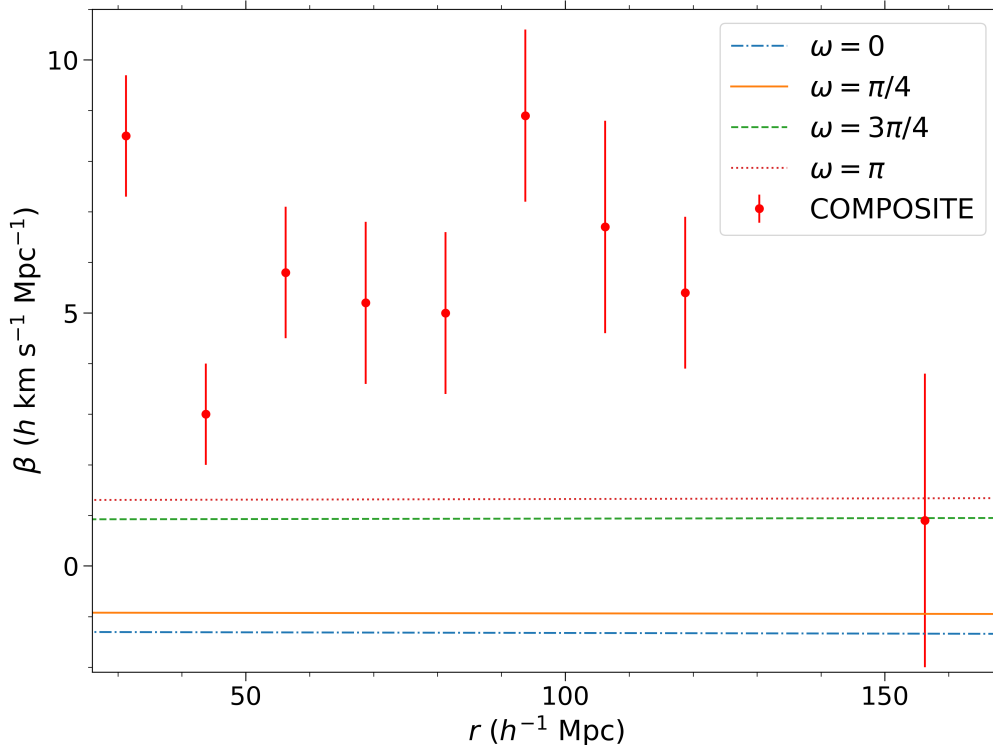


Figure 5. The predicted lower bound on the Hubble constant dipole calculated using the minimum value of amplitude of the perturbation mode that obeys both the NVSS and the CMB constraints obtained in § 6: $(\alpha, \kappa/H_0) = (0.381, 0.043)$ for $\omega = 0, \pi/4, 3\pi/4, \pi$. The dipole values and errors obtained by Wiltshire et al. 2013 [46], using the COMPOSITE Survey, in the CMB rest frame are shown by the red dots and the vertical red error bars. Here r is the comoving distance.

8.1 Dipole Distribution in Galaxy Surveys

An interesting property of our model is that the dipole has a significant redshift dependence. Therefore, the observed dipole value also depends on the redshift range one is looking at. The net dipole distribution as a function of redshift is $D_{\text{kin}} + D_{\text{grav}} + D_{\text{int}}$, with D_{kin} , D_{grav} and D_{int} as defined in Eq. 5.19, Eq. 5.23 and Eq. 5.26, respectively. Figure 6 shows the plot of the dipole distribution with redshift for $\alpha = 0.381$, $\kappa = 0.043H_0$ and $\omega = \pi$ (the smallest fit value of α obtained in § 6).

We also obtain the minimum expected projected dipole amplitudes in three redshift bins, viz., $z = 0.0 - 0.5$, $0.5 - 1.0$ and $1.0 - 2.0$. We use Eq. 5.29 with z_1 and z_2 as the minimum and maximum redshift values of a bin, respectively. Here too, we use the smallest fit value of the perturbation amplitude that obeys both the NVSS and the CMB constraints. These predicted minimum dipole amplitudes have been tabulated in Table 2. This prediction can be tested in future radio and optical surveys.

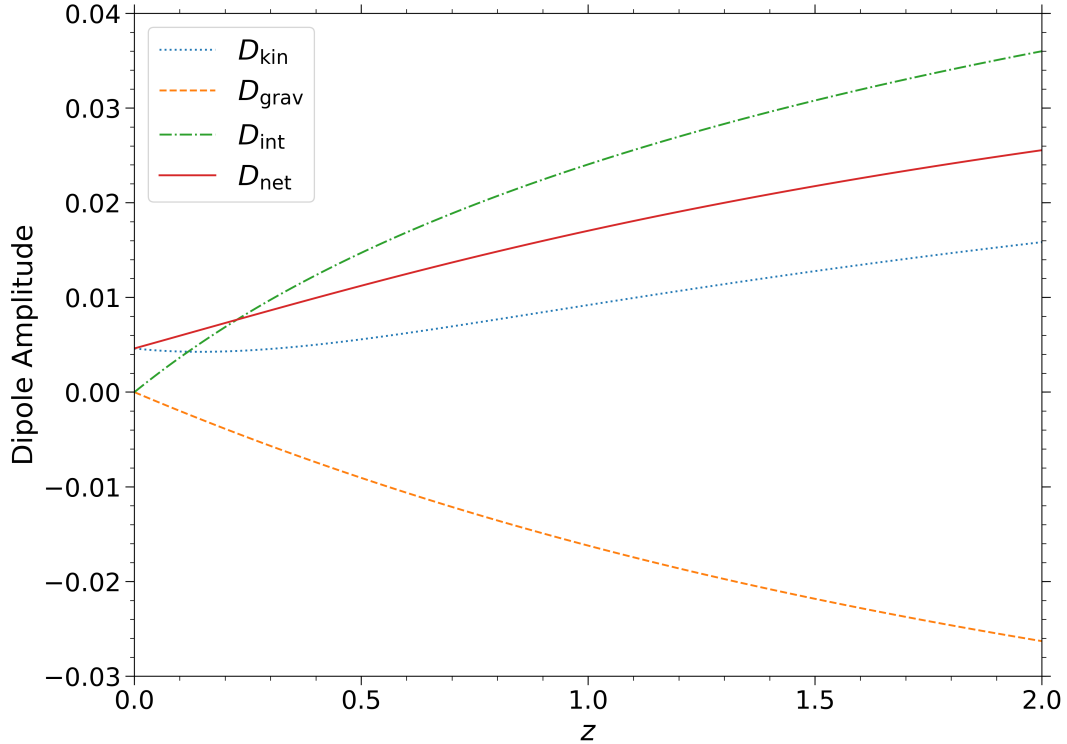


Figure 6. The predicted dipole distribution with redshift assuming the minimum amplitude of the perturbation mode that obeys both the NVSS and the CMB constraints obtained in § 6: $(\alpha, \kappa/H_0, \omega) = (0.381, 0.043, \pi)$.

Redshift bin	Dipole Amplitude D_0
0.0 - 0.5	0.0086
0.5 - 1.0	0.0141
1.0 - 2.0	0.0209

Table 2. Projected dipole prediction for various redshift bins assuming the minimum amplitude of the perturbation mode that obeys both the NVSS and the CMB constraints obtained in § 6: $(\alpha, \kappa/H_0, \omega) = (0.381, 0.043, \pi)$.

8.2 Radio Dipole Prediction for Higher Redshifts

Another test for our model would be to verify the prediction for the minimum expected radio dipole for a survey depth of $z \sim 3$ through future surveys. We use Eq. 5.29, assuming that Eq. 6.1 is valid till $z = 3$, to obtain the predicted value. Using the smallest fit value for the amplitude of the perturbation, we find that the minimum expected dipole would be

0.0164. Note that for predicting the dipole at even higher redshifts, the suppression factor $g(a) = \Psi(a)/\Psi_p$, given by Eq. 2.2, has to be replaced by the numerical solution to Equation 11 in Erickcek et al. 2008 [38].

8.3 Predictions for Anisotropy in the Observed Redshift

As seen in § 7, the superhorizon perturbation introduces an anisotropy in the observed redshift, which can be modelled as $z_{\text{obs}} = \bar{z} + \gamma \cos \theta$, with γ given by Eq. 7.3. We can test for this anisotropy in the present and future supernova and large scale structure surveys. In Figure 7, we plot $\gamma/(H_0 d_L)$ as a function of the luminosity distance d_L in the solar as well as the CMB frame for four different values of ω , viz., $\omega = 0, \pi/4, 3\pi/4$ and π . The values of α and κ used are 0.381 and $0.043H_0$, respectively. We observe that the dipole anisotropy as a function of the luminosity distance saturates at large distances in both the CMB and the solar frame.

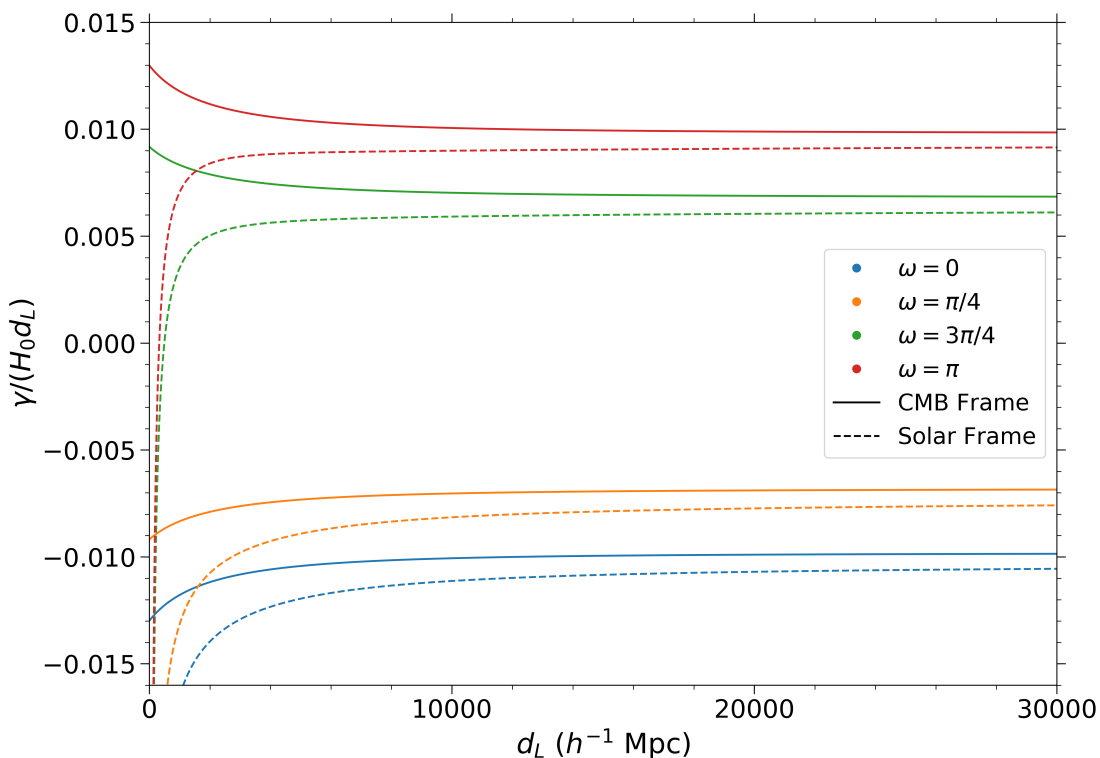


Figure 7. The predicted dipole anisotropy $\gamma/(H_0 d_L)$ in the observed redshift as a function of the luminosity distance d_L . We use the minimum amplitude of the perturbation mode that obeys both the NVSS and the CMB constraints obtained in § 6: $(\alpha, \kappa/H_0) = (0.381, 0.043)$ for $\omega = 0, \pi/4, 3\pi/4, \pi$. We note from Eq. 7.3 that for $z \rightarrow 0$, $\gamma \rightarrow 0$ in the CMB frame ($v_{\text{local}} = 0$), while $\gamma \rightarrow \sim -0.001$ in the solar frame ($v_{\text{local}} \neq 0$).

9 Conclusion

In this paper, we have performed a detailed study of the implications of a superhorizon mode proposed to explain some cosmological observations that appear to show deviation from isotropy. In particular, we show that this mode predicts an extra velocity component of the solar system with respect to the large scale structure. This extra velocity component cancels in the case of CMB but not for large scale structure. This leads to the interesting implication that, within this model's framework, our velocity with respect to the large scale structure is not the same as that with respect to the CMB. The observed value of the dipole anisotropy with respect to large scale structure, however, depends not only on the relative velocity but also on the anisotropic potential induced by the mode and the gravitational redshift induced by this potential. Considering all these contributions, we obtain the parameter range that satisfies both the NVSS observation and the CMB constraints. We also test predictions of the model for the dipole anisotropy in Hubble constant and the Hubble flow bulk velocity in the local universe. The model predicts a small anisotropy in the Hubble constant which is consistent with observations. The observed Hubble flow velocities show considerable spread but are generally found to be smaller than our velocity with respect to the CMB. We also find that our model predicts a velocity of 341 km/s, which is roughly consistent with the observed values.

We show that the superhorizon mode makes several interesting predictions which can be tested in future surveys. In particular, it leads to a remarkable prediction that the dipole in large scale structure should increase with redshift. This increase is expected to saturate only at rather large values of redshift. Similar anisotropic behaviour, which increases with redshift, is predicted for many other observables. In particular, we have demonstrated this for the Hubble parameter dipole and for the observed redshift dipole as a function of distance in the CMB frame. It will be exciting to test these predictions in future observations.

Acknowledgments

We thank Shamik Ghosh for useful comments. We acknowledge funding from the Science and Engineering Research Board (SERB), Government of India, grant number EMR/2016/004070.

References

- [1] R. M. Wald, *Asymptotic behavior of homogeneous cosmological models in the presence of a positive cosmological constant*, *Phys. Rev. D* **28** (1983) 2118.
- [2] J. Dunkley, E. Komatsu, M. R.olta, D. N. Spergel, D. Larson, G. Hinshaw et al., *Five-Year Wilkinson Microwave Anisotropy Probe Observations*, *The Astrophysical Journal Supplement Series* **180** (2009) 306 [0803.0586].
- [3] A. de Oliveira-Costa, M. Tegmark, M. Zaldarriaga and A. Hamilton, *Significance of the largest scale CMB fluctuations in WMAP*, *Phys. Rev. D* **69** (2004) 063516 [astro-ph/0307282].
- [4] N. Aghanim, C. Armitage-Caplan, M. Arnaud, M. Ashdown, F. Atrio-Barandela, J. Aumont et al., *Planck 2013 results. XXIII. Isotropy and statistics of the CMB*, *A&A* **571** (2014) A23 [1303.5083].
- [5] P. Jain and J. P. Ralston, *Anisotropy in the Propagation of Radio Polarizations from Cosmologically Distant Galaxies*, *Modern Physics Letters A* **14** (1999) 417 [astro-ph/9803164].

- [6] J. P. Ralston and P. Jain, *The Virgo Alignment Puzzle in Propagation of Radiation on Cosmological Scales*, *International Journal of Modern Physics D* **13** (2004) 1857 [[astro-ph/0311430](#)].
- [7] D. Hutsemékers, *Evidence for very large-scale coherent orientations of quasar polarization vectors*, *Astronomy & Astrophysics* **332** (1998) 410.
- [8] A. Kogut, C. Lineweaver, G. F. Smoot, C. L. Bennett, A. Banday, N. W. Boggess et al., *Dipole Anisotropy in the COBE Differential Microwave Radiometers First-Year Sky Maps*, *ApJ* **419** (1993) 1 [[astro-ph/9312056](#)].
- [9] G. Hinshaw, J. L. Weiland, R. S. Hill, N. Odegard, D. Larson, C. L. Bennett et al., *Five-Year Wilkinson Microwave Anisotropy Probe Observations: Data Processing, Sky Maps, and Basic Results*, *ApJS* **180** (2009) 225 [[0803.0732](#)].
- [10] Planck Collaboration, Y. Akrami and A. et. al, *Planck 2018 results. I. Overview and the cosmological legacy of Planck*, *arXiv e-prints* (2018) arXiv:1807.06205 [[1807.06205](#)].
- [11] Planck Collaboration, N. Aghanim and Y. e. a. Akrami, *Planck 2018 results. III. High Frequency Instrument data processing and frequency maps*, *arXiv e-prints* (2018) arXiv:1807.06207 [[1807.06207](#)].
- [12] M. J. Hudson, R. J. Smith, J. R. Lucey and E. Branchini, *Streaming motions of galaxy clusters within 12000 km s⁻¹. The peculiar velocity field*, *MNRAS* **352** (2004) 61 [[astro-ph/0404386](#)].
- [13] R. Watkins, H. A. Feldman and M. J. Hudson, *Consistently large cosmic flows on scales of 100 h1 Mpc: a challenge for the standard Λ CDM cosmology*, *MNRAS* **392** (2008) 743 [[0809.4041](#)].
- [14] R. Watkins and H. A. Feldman, *Large-scale bulk flows from the Cosmicflows-2 catalogue*, *MNRAS* **447** (2014) 132 [[1407.6940](#)].
- [15] G. Lavaux, R. B. Tully, R. Mohayaee and S. Colombi, *Cosmic Flow From Two Micron All-Sky Redshift Survey: the Origin of Cosmic Microwave Background Dipole and Implications for Λ CDM Cosmology*, *ApJ* **709** (2010) 483 [[0810.3658](#)].
- [16] H. A. Feldman, R. Watkins and M. J. Hudson, *Cosmic flows on 100 h1 Mpc scales: standardized minimum variance bulk flow, shear and octupole moments*, *MNRAS* **407** (2010) 2328 [[0911.5516](#)].
- [17] Feindt, U., Kerschhaggl, M., Kowalski, M., Aldering, G., Antilogus, P., Aragon, C. et al., *Measuring cosmic bulk flows with type ia supernovae from the nearby supernova factory*, *A&A* **560** (2013) A90.
- [18] J. J. Condon, W. D. Cotton, E. W. Greisen, Q. F. Yin, R. A. Perley, G. B. Taylor et al., *The NRAO VLA Sky Survey*, *AJ* **115** (1998) 1693.
- [19] T. Mauch, T. Murphy, H. J. Buttery, J. Curran, R. W. Hunstead, B. Piestrzynski et al., *SUMSS: a wide-field radio imaging survey of the southern sky - II. The source catalogue*, *MNRAS* **342** (2003) 1117 [[astro-ph/0303188](#)].
- [20] H. T. Intema, P. Jagannathan, K. P. Mooley and D. A. Frail, *The GMRT 150 MHz all-sky radio survey. First alternative data release TGSS ADR1*, *A&A* **598** (2017) A78 [[1603.04368](#)].
- [21] R. J. Wilman, L. Miller, M. J. Jarvis, T. Mauch, F. Levrier, F. B. Abdalla et al., *A semi-empirical simulation of the extragalactic radio continuum sky for next generation radio telescopes*, *MNRAS* **388** (2008) 1335 [[0805.3413](#)].
- [22] G. F. R. Ellis and J. E. Baldwin, *On the expected anisotropy of radio source counts*, *MNRAS* **206** (1984) 377.
- [23] C. Blake and J. Wall, *A velocity dipole in the distribution of radio galaxies*, *Nature* **416** (2002) 150.

- [24] A. K. Singal, *Large Peculiar Motion of the Solar System from the Dipole Anisotropy in Sky Brightness due to Distant Radio Sources*, *ApJ* **742** (2011) L23 [[1110.6260](#)].
- [25] C. Gibelyou and D. Huterer, *Dipoles in the sky*, *MNRAS* **427** (2012) 1994 [[1205.6476](#)].
- [26] M. Rubart and D. J. Schwarz, *Cosmic radio dipole from NVSS and WENSS*, *A&A* **555** (2013) A117 [[1301.5559](#)].
- [27] P. Tiwari, R. Kothari, A. Naskar, S. Nadkarni-Ghosh and P. Jain, *Dipole anisotropy in sky brightness and source count distribution in radio NVSS data*, *Astroparticle Physics* **61** (2015) 1 [[1307.1947](#)].
- [28] P. Tiwari and P. Jain, *Dipole anisotropy in integrated linearly polarized flux density in NVSS data*, *MNRAS* **447** (2015) 2658 [[1308.3970](#)].
- [29] P. Tiwari and A. Nusser, *Revisiting the NVSS number count dipole*, *Journal of Cosmology and Astroparticle Physics* **2016** (2016) 062.
- [30] J. Colin, R. Mohayaee, M. Rameez and S. Sarkar, *High-redshift radio galaxies and divergence from the CMB dipole*, *MNRAS* **471** (2017) 1045 [[1703.09376](#)].
- [31] C. A. P. Bengaly, R. Maartens and M. G. Santos, *Probing the Cosmological Principle in the counts of radio galaxies at different frequencies*, *JCAP* **2018** (2018) 031 [[1710.08804](#)].
- [32] A. K. Singal, *Large disparity in cosmic reference frames determined from the sky distributions of radio sources and the microwave background radiation*, *Phys. Rev. D* **100** (2019) 063501 [[1904.11362](#)].
- [33] A. Dolfi, E. Branchini, M. Bilicki, A. Balaguera-Antolínez, I. Prandoni and R. Pandit, *Clustering properties of TGSS radio sources*, *A&A* **623** (2019) A148 [[1901.08357](#)].
- [34] P. Tiwari, S. Ghosh and P. Jain, *The galaxy power spectrum from TGSS ADR1 and the effect of flux calibration systematics*, *Astrophys. J.* **887** (2019) 175 [[1907.10305](#)].
- [35] C. Gordon, W. Hu, D. Huterer and T. M. Crawford, *Spontaneous isotropy breaking: a mechanism for cmb multipole alignments*, *Phys. Rev. D* **72** (2005) 103002 [[astro-ph/0509301](#)].
- [36] C. Gordon, *Broken Isotropy from a Linear Modulation of the Primordial Perturbations*, *Astrophys. J.* **656** (2007) 636 [[astro-ph/0607423](#)].
- [37] A. L. Erickcek, M. Kamionkowski and S. M. Carroll, *A hemispherical power asymmetry from inflation*, *Phys. Rev. D* **78** (2008) 123520 [[0806.0377](#)].
- [38] A. L. Erickcek, S. M. Carroll and M. Kamionkowski, *Superhorizon perturbations and the cosmic microwave background*, *Phys. Rev. D* **78** (2008) 083012 [[0808.1570](#)].
- [39] S. Ghosh, *Generating intrinsic dipole anisotropy in the large scale structures*, *Phys. Rev. D* **89** (2014) 063518 [[1309.6547](#)].
- [40] L. P. Grishchuk and I. B. Zeldovich, *Long-wavelength perturbations of a Friedmann universe, and anisotropy of the microwave background radiation*, *Soviet Astronomy* **22** (1978) 125.
- [41] M. S. Turner, *Tilted universe and other remnants of the preinflationary universe*, *Phys. Rev. D* **44** (1991) 3737.
- [42] M. Bruni and D. H. Lyth, *Peculiar velocity, cosmic perturbation theory and the cosmic microwave background anisotropy*, *Physics Letters B* **323** (1994) 118 [[astro-ph/9307036](#)].
- [43] Planck Collaboration, N. Aghanim, Y. Akrami, M. Ashdown, J. Aumont, C. Baccigalupi et al., *Planck 2018 results. VI. Cosmological parameters*, *arXiv e-prints* (2018) arXiv:1807.06209 [[1807.06209](#)].
- [44] S. Dodelson, *Modern cosmology*. Academic Press, 2003.
- [45] D. S. Gorbunov and V. A. Rubakov, *Introduction to the theory of the early universe*. World Scientific, 2011.

- [46] D. L. Wiltshire, P. R. Smale, T. Mattsson and R. Watkins, *Hubble flow variance and the cosmic rest frame*, *Phys. Rev. D* **88** (2013) 083529 [[1201.5371](#)].
- [47] C. B. Jr., *Constraining the local variance of H_0 from directional analyses*, *Journal of Cosmology and Astroparticle Physics* **2016** (2016) 036 [[1510.05545](#)].
- [48] J. Colin, R. Mohayaee, S. Sarkar and A. Shafieloo, *Probing the anisotropic local Universe and beyond with SNe Ia data*, *MNRAS* **414** (2011) 264 [[1011.6292](#)].
- [49] D.-C. Dai, W. H. Kinney and D. Stojkovic, *Measuring the cosmological bulk flow using the peculiar velocities of supernovae*, *JCAP* **2011** (2011) 015 [[1102.0800](#)].
- [50] B. Rathaus, E. D. Kovetz and N. Itzhaki, *Studying the peculiar velocity bulk flow in a sparse survey of Type Ia SNe*, *MNRAS* **431** (2013) 3678 [[1301.7710](#)].
- [51] G. J. Mathews, B. M. Rose, P. M. Garnavich, D. G. Yamazaki and T. Kajino, *Detectability of Cosmic Dark Flow in the Type Ia Supernova Redshift–Distance Relation*, *ApJ* **827** (2016) 60 [[1412.1529](#)].
- [52] S. Appleby, A. Shafieloo and A. Johnson, *Probing Bulk Flow with Nearby SNe Ia Data*, *ApJ* **801** (2015) 76 [[1410.5562](#)].